Strain-Driven Stacking Faults in CdSe/CdS Core/Shell Nanorods

Arnaud Demortière,*,[†,‡,§] Donovan N. Leonard,[∥] Valeri Petkov,[⊥] Karena Chapman,[#]
Soma Chattopadhyay,[#] Chunxing She,[†] David A. Cullen,[∥] Tomohiro Shibata,[#] Matthew Pelton,*,[†,∇]
and Elena V. Shevchenko[†]

[†]Center for Nanoscale Materials, Argonne National Laboratory, 9700 South Cass Avenue, Argonne, Illinois 60439, United States
[‡]Laboratoire de Réactivité et Chimie des Solides (LRCS), CNRS UMR 7314, Université Picardie Jules Verne, 80039 Amiens, France
[§]Réseau sur le Stockage Electrochimique de l'Energie (RS2E), CNRS FR 3459, 80039 Amiens, France
[∥]Materials Science and Technology Division, Oak Ridge National Laboratory, 1 Bethel Valley Road, Oak Ridge, Tennessee 37831-6071, United States
[⊥]Department of Physics, Central Michigan University, Mount Pleasant, Michigan 48859, United States
[#]Advanced Photon Source, Argonne National Laboratory, 9700 South Cass Avenue, Argonne, Illinois 60439, United States
[∇]Department of Physics, University of Maryland, Baltimore County (UMBC), Baltimore, Maryland 21250, United States

S Supporting Information

ABSTRACT: Colloidal semiconductor nanocrystals are commonly grown with a shell of a second semiconductor material to obtain desired physical properties, such as increased photoluminescence quantum yield. However, the growth of a lattice-mismatched shell results in strain within the nanocrystal, and this strain has the potential to produce crystalline defects. Here, we study CdSe/CdS core/shell nanorods as a model system to investigate the influence of core size and shape on the formation of stacking faults in the nanocrystal. Using a combination of high-angle annular dark-field scanning transmission electron microscopy and pair-distribution-function analysis of synchrotron X-ray scattering, we show that growth of the CdS shell on smaller, spherical CdSe cores results in relatively small strain and few stacking faults. By contrast, growth of the shell on larger, prolate spheroidal cores leads to significant strain in the CdS lattice, resulting in a high density of stacking faults.
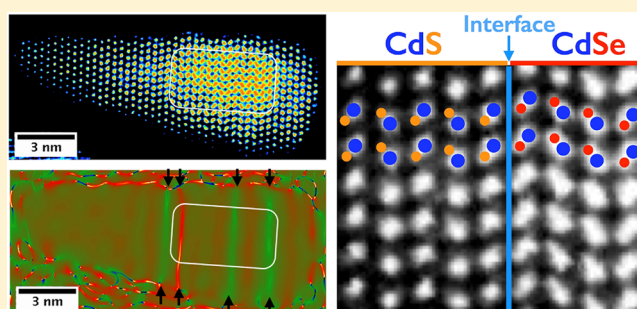
Colloidal semiconductor nanocrystals are a versatile class of materials that have size-tunable emission wavelengths across the visible and infrared spectral ranges and exhibit large molar absorption coefficients as well as high photostability compared to typical organic luminophores.[1−3] Core−shell nanocrystals, in which an epitaxial shell of a wider-bandgap semiconductor is grown around a core of a narrower-bandgap semiconductor, are commonly used for optical applications, because the shell can increase luminescence efficiency, and can also control other processes such as Auger recombination and blinking.[4−9]

However, the core and shell materials generally have different lattice constants, and this lattice mismatch gives rise to stress during the growth of the shell. For conventional planar growth,[10] a lattice-mismatched epitaxial layer grows coherently (dislocation-free) below a critical thickness, corresponding to a maximum of elastic energy density, above which stress is released through the formation of misfit dislocations and roughening of the surface.[11,12] For core−shell nanocrystals, by contrast, the role of stress is complicated by the three-dimensional geometry of the growth surface[13] and the small volume of the shell. Stress is distributed in both the core and the shell;[14,15] for example, the deposition of 7.5 monolayers of ZnS on a spherical CdS nanocrystals was found to be equivalent to applying a hydrostatic pressure of 4 GPa on the core.[16] Small cores can deform under this stress; for example, growth of a CdS shell on a CdSe core, with a lattice mismatch of 3.9%, was observed to produce a compressive strain of 0.6% that increases with the thickness of the shell.[17] For larger cores or thicker shells, the high lattice strain energy that is required for an ideal shell may be relieved by the formation of crystalline defects.[18] One study has reported that CdS shells grow uniformly on CdSe cores only below a certain critical thickness, after which the shells become irregular, in a situation similar to planar epitaxial growth.[19] Strain-induced defects have the potential to reduce luminescence efficiency through the creation of states that assist nonradiative recombination.[20,21]

A particularly informative system for studies of the formation of crystalline defects are CdSe/CdS core/shell nanocrystals with small, spherical or spheroidal cores and larger, rod-shaped shells,[22,23] because a single growth step can produce shells with controlled dimensions that extend up to sizes much larger than the cores. Here, we examine the impact of the CdSe core size on the internal structure of CdSe/CdS core/shell nanorods. CdSe/CdS heterostructures with different core sizes but equal volumes were synthesized following a modification of the previously reported seeded growth process[22,24] In this Letter, we focus on nanorods with two core sizes: (1) large, prolate spheroidal shells with a long axis of 5.0 nm and a short axis of 3.5 nm (referred to as 5 nm cores), and (2) small, spherical cores with a diameter of 2.0 nm (referred to as 2 nm cores). Figure 1a,b shows representative transmission electron micro-
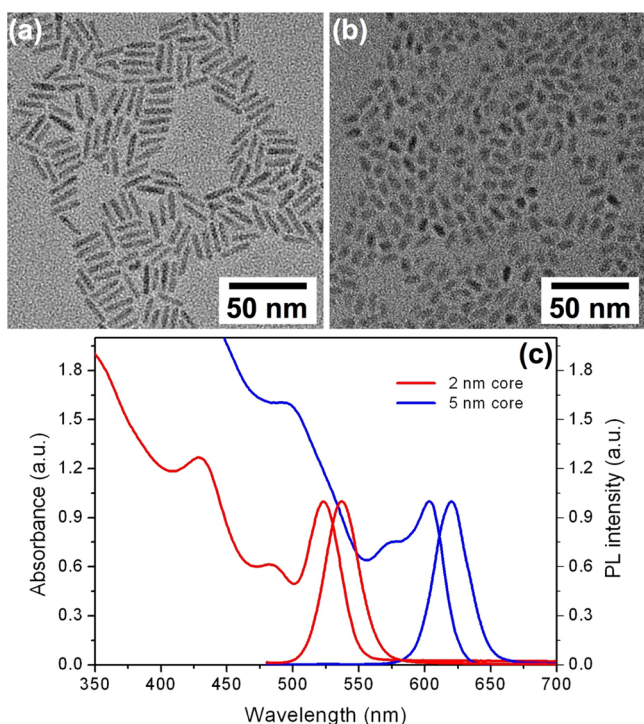

Figure 1. (a,b) Transmission electron microscope (TEM) images of CdSe/CdS core/shell nanorods with (a) 2 nm cores and (b) 5 nm cores. (c) Normalized photoluminescence (PL) and absorbance spectra for CdSe/CdS nanorods with 2 nm cores and 5 nm cores in toluene. PL spectra were obtained for an excitation wavelength of 450 nm.

scope (TEM) images of the two core/shell nanorod samples; the high morphological uniformity of the samples is apparent from the images. The monodispersity of the samples is also consistent with the narrow line widths (5−6%) of the photoluminescence (PL) and absorption spectra (see Figure 1c).

To gain insight into the structure of the CdSe/CdS nanorods, we obtained atomic-resolution images using an aberration-corrected scanning transmission electron microscope (STEM, NION UltraSTEM 100-Cs) equipped with a cold field emission gun. In high-resolution STEM mode, the high-angle annular dark-field (HAADF) detector allows us to analyze the crystals via Z-contrast imaging by capturing scattered electrons at specific angles. Figure 2a shows a representative image for a CdSe/CdS nanorod with a 5 nm

core. The intensity of the scattered electrons at the high angles collected in HAADF-STEM is proportional to Z^{α}, where Z is the atomic number and α is a constant in the range of 1.6−1.9 for most cases.[25] Contrast variations in the atomic-resolution images can thus be used to delineate the CdSe core structure embedded within the CdS shell, due to the weaker scattering cross-section of sulfur atoms compared to selenium atoms (see Figure 2b,c).[26] The off-center position of the core is in agreement with previously reported data.[22,27] The tapering of the nanorod diameter is a result of the fast anisotropic growth of the CdS shell.[28] The CdSe core position can also be visualized by calculating a fast Fourier transform (FFT) of the image (Figure 2d), masking the portion of the FFT corresponding to the CdS lattice, and performing an inverse transform. In the resulting Fourier filtered image (Figure 2e), the blue color corresponds to the region around the CdSe core.

Note that the FFT pattern exhibits the expected reflections characteristic of the Wurtzite structure; however, additional well-resolved features (indicated by the arrows in Figure 2d) are also present. These extra spots can be indicative of planar defects such as twin deformations induced by stacking faults. By contrast, the FFT pattern obtained from the CdS shell area remote from the CdSe core exhibits only regular spots characteristic of the Wurzite structure, without satellite peaks.

To determine whether the additional spots in the FFT patterns do in fact correspond to stacking faults, we map the shear strain within the nanoparticle using geometric phase analysis (GPA). In this method, displacements of atomic positions in the Fourier-filtered image are analyzed relative to an internal reference area. We calculated images of shear strain, S_{xy}, by Fourier filtering using spots corresponding to the $[0001]$ and $[10\overline{1}0]$ directions, along and perpendicular to the nanorod, respectively. The radius chosen in Fourier space for the Gaussian filter and the pixel size of the original HAADF-STEM image result in an accuracy of approximately 0.05% in determination of strain.[29] The result, shown in Figure 2f, exhibits three clear strain lines around the core/shell interface and one within the core. A similar analysis enables imaging of in-plane rotation, R_{xy}; as shown in the Supporting Information (Figure S1), this analysis shows strain lines located at identical positions within the nanorod. This combination of shear and rotational strain is consistent with the presence of stacking faults.

Identification of the stacking faults can be further confirmed by Fourier filtering of the HAADF-STEM images using additional features in the FFT pattern (Figure 2d) related to the presence of the crystalline defects. As shown in Figure 3a,b, the resulting Fourier-filtered image shows lines that correspond to the positions of the strain lines revealed by the GPA analysis. Closer analysis of the HAADF-STEM image near the CdSe/CdS interface shows a clear displacement in atomic positions, corresponding to the accumulation of lattice strain at the interface (see Figure 3c,d). This suggests that the stacking faults form due to the strain that accumulates during the growth of the lattice-mismatched shell. This interpretation is further supported by examining high-resolution TEM images of 5.0 nm CdSe seeds prior to the CdS shell growth (see Supporting Information Figure S2): these images show no stacking faults, indicating that the stacking faults arise during the growth of the CdS shell.

Equivalent HAADF-STEM imaging and analysis was performed for CdSe/CdS core/shell nanorods with 2 nm cores. Results for a characteristic nanorod are shown in Figure
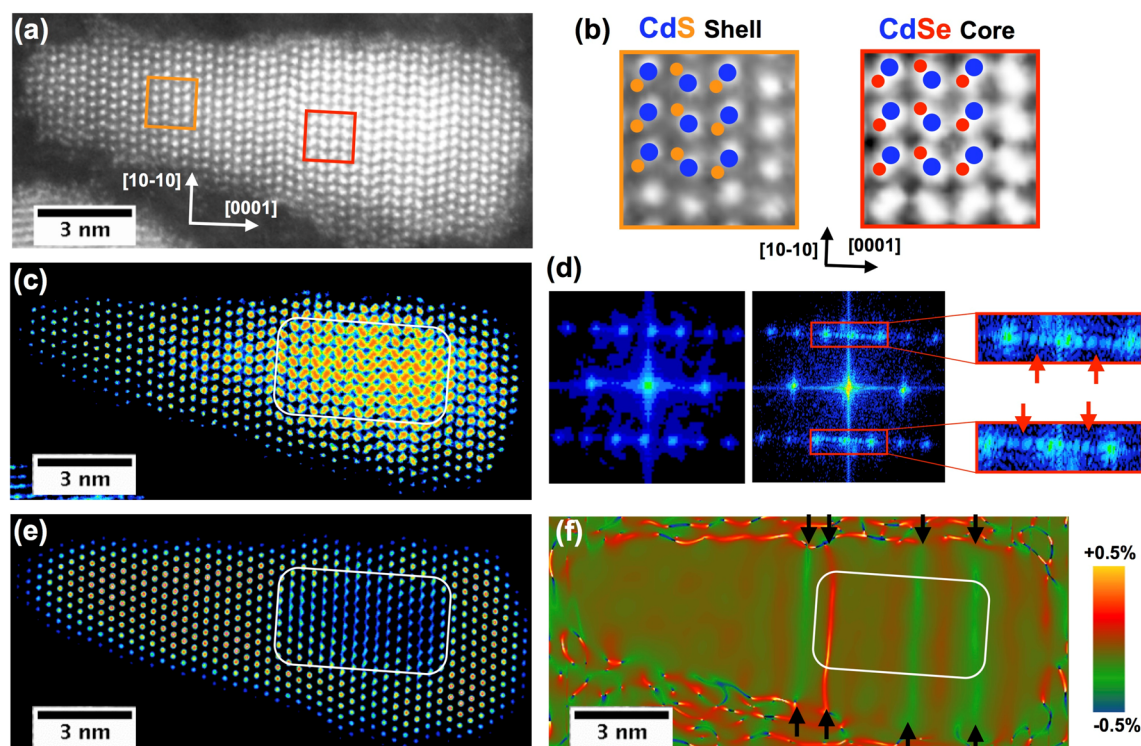
Figure 2. (a) High-angle annular dark-field scanning transmission electron microscope (HAADF-STEM) image of a CdSe/CdS core/shell nanorod with a 5 nm prolate CdSe core. (b) Magnified images of areas indicated in (a) demonstrating the atomic structures of the CdS shell and the CdSe core. Cd atoms are depicted in blue, S atoms in orange, and Se atoms in red. (c) False-color amplitude image. The white line is a guide for the eye indicating the approximate boundary of the CdSe core. (d) Fast Fourier transform (FFT) patterns obtained from the entire nanoparticle (left) and from the CdS shell only (right). Magnified areas from the right-hand image show satellite peaks, indicated by red arrows. (e) False-color FFT-filtered image using the FFT pattern of CdSe as a mask. (f) False-color image obtained by geometric phase analysis (GPA), depicting the displacement in the directions perpendicular ($[10\bar{1}0]$) and parallel ($[0001]$) to the long axis of the nanorod. Color variation from blue to orange corresponds to strains from -0.5% to 0.5%.
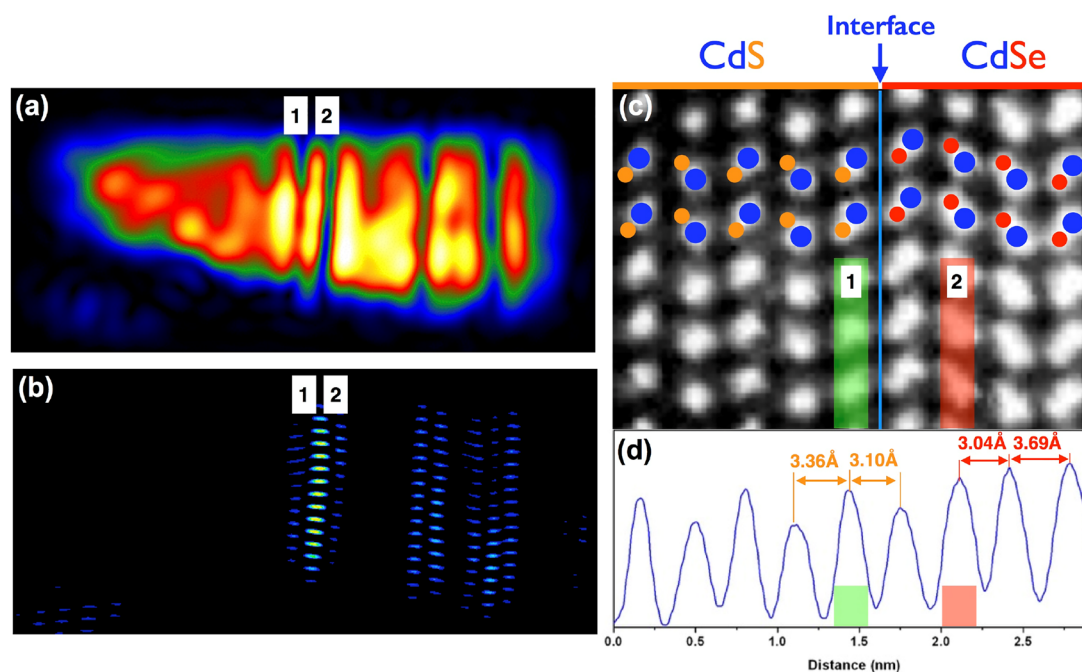

Figure 3. (a) Image of the amplitude of the fast Fourier transform (FFT) reflection used for the geometric phase analysis (GPA) analysis shown in Figure 2f. (b) FFT-filtered image using the FFT of CdSe and CdS as masks. The remaining atomic lines coincide with strain lines seen in the GPA image. (c) Magnification of a high-resolution HAADF-STEM image near the CdSe/CdS interface (indicated by the arrow). Cd atoms are depicted in blue, S atoms in orange, and Se atoms in red. (d) Intensity profile showing atomic displacement near the interface.
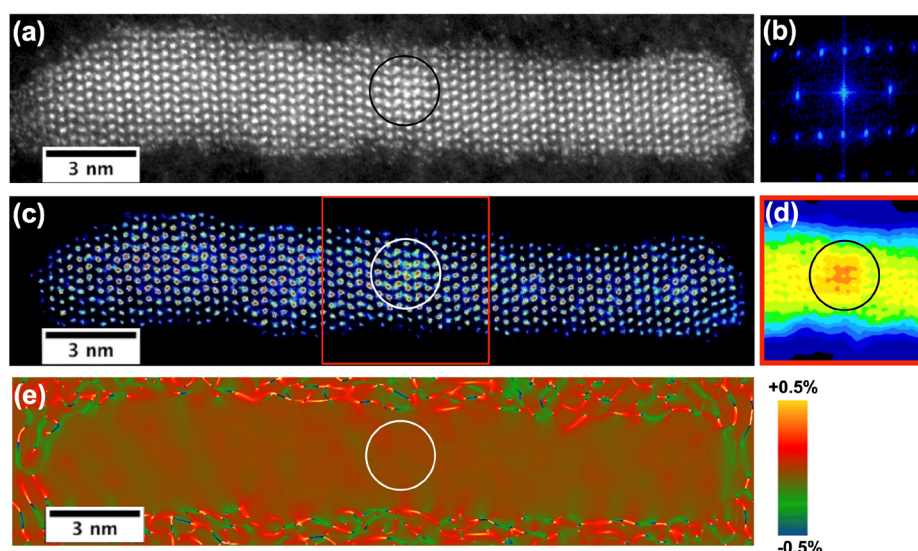
Figure 4. (a) High-angle annular dark-field scanning transmission electron microscope (HAADF-STEM) image of a CdSe/CdS core/shell nanorod with a 2 nm spherical CdSe core. The black line is a guide for the eye indicating the approximate boundary of the CdSe core. (b) Fast Fourier transform (FFT) pattern from the HAADF-STEM image. (c) False-color amplitude image. (d) Magnified false-color image of the central area of the nanorod, indicated by the red square in panel c. (e) False-color image obtained by geometric phase analysis (GPA).
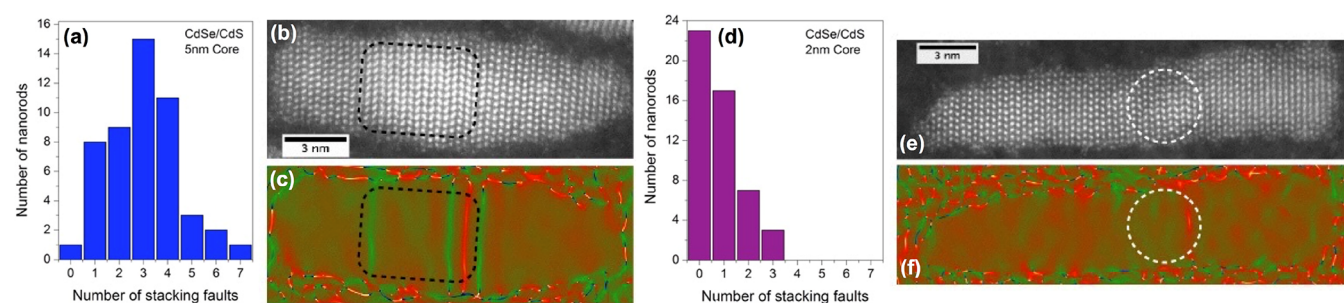

Figure 5. (a) Distribution of the number of stacking faults obtained by geometric phase analysis (GPA) of high-angle annular dark-field scanning transmission electron microscope (HAADF-STEM) images for 50 CdSe/CdS core/shell nanorods with 5 nm CdSe cores. (b) HAADF-STEM image of a representative nanorod with a 5 nm core. (c) Strain image of the nanorod obtained by GPA. (d) Distribution of the number of stacking faults for 50 nanorods with 2 nm cores. (e) HAADF-STEM image of a representative nanorod with a 2 nm core. (f) Corresponding strain image from GPA.

Table 1. Lattice Parameters, a and c, and Corresponding Fractional Deviations from Bulk Lattice Parameters, Obtained from Analysis of Pair Distribution Functions (PDFs) for X-ray Scattering from CdSe Nanocrystals and CdSe/CdS Core/Shell Nanorods

		CdSe				CdS			
core size	sample	a_{CdSe} (Å)	$\Delta a/a_{bulk}$	c_{CdSe} (Å)	$\Delta c/c_{bulk}$	a_{CdS} (Å)	$\Delta a/a_{bulk}$	c_{CdS} (Å)	$\Delta c/c_{bulk}$
2.0 nm	CdSe	4.281 ± 0.008	−0.40%	6.987 ± 0.026	−0.37%				
	CdSe/CdS	4.231 ± 0.003	−1.56%	6.971 ± 0.008	−0.60%	4.110 ± 0.002	−0.63%	6.690 ± 0.005	−0.36%
5.0 nm	CdSe	4.290 ± 0.006	−0.19%	6.974 ± 0.016	−0.55%				
	CdSe/CdS	4.270 ± 0.006	−0.65%	6.981 ± 0.019	−0.46%	4.223 ± 0.008	2.10%	6.886 ± 0.006	2.56%

4, and reveal no stacking faults within the nanorod. Additional results are shown in the Supporting Information (Figure S3).

The results obtained for 50 nanorods with 5 nm cores and 50 nanorods with 2 nm cores are summarized in Figure 5, together with images and shear-strain maps for additional characteristic examples. Nanorods with 5 nm cores have an average of 3 stacking faults each, whereas rods with 2 nm cores have an average of less than one stacking fault each, with almost half of the nanorods having no stacking faults.

The HAADF-STEM results indicate that CdSe/CdS nanorods with large CdSe cores contain multiple stacking faults, whereas nanorods with small cores are mostly free of stacking faults. The results also suggest that the stacking faults arise from strain that accumulates during the growth of the CdS shell. To quantify this strain and average over a larger number of nanorods, we measured synchrotron X-ray scattering from ensembles of nanorods and analyzed the resulting pair distribution functions (PDFs). Experimental results are shown in Supporting Information Figure S4. The measured PDFs were fit to models that assume a single nanophase for the CdSe cores and two distinct nanophases for the core/shell nanorods, resulting in the lattice parameters given in Table 1.

The results indicate that the CdSe cores by themselves are compressed anisotropically, most likely due to anisotropic

elastic properties of the crystal lattice. After deposition of the CdS shell, the CdSe cores further contract to match the smaller lattice constant of the overgrown CdS. However, the strain in the CdS shell is very different for the two different core sizes. For nanorods with 2 nm cores, the lattice parameters of the CdS shell are slightly smaller than the bulk lattice parameters. In this case, the volume of the shell is much larger than that of the core, and its interior is largely undisturbed by the small CdSe core. For nanorods with 5 nm cores, by contrast, the volumes of the core and shell are similar to one another, leading to significant expansion of the lattice parameters of the shell. This means that significant stress accumulates during the growth of CdS shells around the 5 nm cores; the observed stacking faults most likely form to relieve this stress. The observation that more strain accumulates for CdS growth around larger cores is consistent with previous reports that the elastic modulus of CdSe nanocrystals is a size-dependent parameter that exhibits lower values for smaller sizes.[30]

Our observations are also consistent with previous observations that the formation of twin boundaries at the nanoscale is strongly driven by the size and shape of the seed/matrix interface.[31] Indeed, the morphology of the CdSe cores appears to play a role in the formation of crystal defects, as well as their size. Stacking faults are known to emerge and extend as planar two-dimensional defects as so to increase crystal stability.[32,33] The prolate shape of larger CdSe cores may therefore be responsible for the observed orientation of stacking faults perpendicular to the long axis of the nanorod (the [0001] crystal direction) and parallel to the CdSe/CdS interface.

We note that the increasing number of planar defects in the nanorods with increasing core size appears to be correlated with a decrease in their photoluminescence quantum yield (PLQY). Supporting Information Figure S5a shows that the measured PLQY decreases for nanorods with different core sizes but nearly identical volumes with increasing core size, with an abrupt drop between 3 nm spherical cores and 4 nm prolate cores. Radiative and nonradiative recombination rates are inferred from these PLQY values and time-resolved photoluminescence measurements, and are summarized in Supporting Information Figure S5b. As expected, radiative rates are the same for nanorods with equal volumes, regardless of core size,[24] apart from a small decrease between core sizes of 3 and 4 nm, where the core shape changes from spherical to prolate spheroidal. By contrast, the nonradiative recombination rate increases continually with increasing core size, with an abrupt increase between core sizes of 3 and 4 nm. Growing a ZnS shell on the nanorods does not affect their PLQY, suggesting that surface defects are not primarily responsible for nonradiative recombination in these structures. The correlation between increased nonradiative recombination and increased number of strain-induced stacking faults suggests an important role of strain-induced structural factors in nonradiative recombination, but further work is required to clarify the connection.

In summary, we have conducted a detailed, atomic-resolution structural study of CdSe/CdS nanorods with different sized cores. Using high-resolution HAADF-STEM and GPA of synchrotron X-ray scattering, we demonstrated that nanorods with larger cores are characterized by higher lattice distortion and a corresponding higher number of stacking faults. The density of stacking faults also appears to be related to the change in shape of the core from spherical to prolate ellipsoidal as it becomes larger. Determining the exact role of the core–

shell interface in the formation of stacking faults will require systematic study of samples with a larger range of core sizes. Future investigations into different core/shell geometries and core/shell nanocrystals comprising different combinations of semiconductors will provide further insight into the origins and generality of these strain-induced defects. Coupling these experimental investigations to atomistic simulations of nanocrystal growth and models of electronic structure will ultimately be required to understand the origins of strain-induced defects and their role in determining the optical properties of the nanocrystals. These studies will ultimately provide insight into the influence of strain on other physical properties of nanocrystals, such as their mechanical properties and their phase transitions under pressure.

■ EXPERIMENTAL METHODS

Synthesis of Semiconductor Nanocrystals. CdO (Sigma-Aldrich, 99%), *n*-propylphosphonic acid (PPA, Sigma-Aldrich, 95%), trioctylphosphine oxide (TOPO, Sigma-Aldrich, 99%), octadecyl-phosphonic acid (ODPA, PCI Synthesis, 97%), trioctylphosphine (TOP, Fluka, 90%), selenium (Sigma-Aldrich, 98%), sulfur (Sigma-Aldrich, 99%), n-propylphosphonic acid (PPA, Sigma-Aldrich, 95%), dodecanoic acid (Sigma-Aldrich, 99%), 1-octadecene (Sigma-Aldrich, 90%), octadecylamine (Sigma-Aldrich, 97%), and octylamine (Sigma-Aldrich, 99%) were used for synthesis of the nanocrystals.

CdSe seeds were synthesized in a 50 mL three-neck flask under a nitrogen environment. TOPO (3.0 g), ODPA (0.308 g), and CdO (0.060 g) were mixed, heated up to 150 °C, and kept under vacuum for 2 h. The reaction solution was then heated under nitrogen to 300 °C at approximately 7 °C/min. The reaction solution became transparent, indicating the formation of Cd-ODPA complexes. Next, 1.5 g of TOP was rapidly injected into the reaction flask. TOP-Se solution (0.058 g Se + 0.360 g TOP) was then injected; for the synthesis of 2.0, 4.0, and 5.0 nm seeds, the injection temperatures were 380 °C, 370 °C, and 360 °C, respectively. For 2.0 nm seeds, the reaction was quenched immediately after the injection of TOP-Se by injection of 5 mL of room-temperature toluene. For 4.0 and 5.0 nm seeds, the reaction solution was kept at high temperature for 330 s. After the solution cooled down to room temperature, the seeds were precipitated by adding ethanol and centrifuging; this washing step was repeated twice. Finally, the seeds were redissolved in toluene and stored inside a glovebox under nitrogen atmosphere.

For synthesis of CdSe/CdS core/shell nanorods, CdO (0.207 g), PPA (0.015 g), TOPO (2.0 g), and ODPA (1.28g) were mixed in a three-neck flask. The solution was degassed, heated up to 150 °C, and kept under vacuum for 2 h. The solution was then heated up to 340 °C and kept at that temperature for 15 min. Next, 1.5 g of TOP was injected. After stabilization of the temperature at 340 °C, TOP-S solution (0.05152 g S + 0.5957 g TOP) and TOP-seeds solution (2 mg CdSe seeds +0.5 mL TOP) were rapidly injected in the flask. The reaction time was varied from 1 to 10 min in order to control the shell size. After the synthesis, the CdSe/CdS nanorods were precipitated with methanol (20 mL) and were then redissolved in toluene (5 mL) containing dodecanoic acid (0.125 g) and octylamine (0.390 g).

For synthesis of CdSe/CdS/ZnS core/shell/shell nanorods, 1-octadecene (3 mL), octadecylamine (1g), and CdSe/CdS nanorods (50 mg) were mixed in a three-neck flask and degassed at 150 °C under vacuum for 1 h. A solution of zinc

with $Zn(AC)_2$ (92.7 mg), oleic acid (1.12 mL), and 1-octadecene (3.75 mL) and a solution of sulfur with S (16 mg) and 1-octadecene (5 mL) were prepared. The initial solution in the three-neck flask was then heated up to 240 °C (under N_2) and kept at that temperature for 15 min. Next, 1 mL of zinc solution and 1 mL of sulfur solution were injected. After stabilization of the temperature at 240 °C, the solution was kept at that temperature for 30 min. After the solution cooled down to room temperature, the nanorods were precipitated by adding ethanol and centrifuging. Finally, the nanorods were redissolved in toluene.

High-Angle Annular Dark Field Scanning Transmission Electron Microscopy. Core/shell nanorods on ultrathin amorphous-carbon grids were imaged using a Nion UltraSTEM 100 (U100) dedicated aberration-corrected STEM Instrument featuring a third-generation C3/C5 aberration corrector, 0.5 nA current in an atomic-size probe, and 1.0−1.1 Å HAADF-STEM imaging resolution at 60 kV and 100 kV operating voltages. A high-angle annular dark-field (HAADF) detector was used to obtain sub-Ångström-resolution images with Z-contrast. Geometric phase analysis (GPA) was performed using Gatan Digital Micrograph software with the FRWRtools plugin.[34]

Pair-Distribution-Function Analysis. Total X-ray scattering experiments were conducted at the 11-ID-B beamline of the Advanced Photon Source at Argonne National Laboratory, using 59 keV X-rays and a large-area detector. Data analysis and calculation of atomic pair distribution functions (PDFs) were carried out using PDF-GETX2 software packages.[35] Structure modeling guided by the experimental PDF data was done with the help of PDFGUI software.[36]

ASSOCIATED CONTENT

ⓈSupporting Information

The Supporting Information is available free of charge on the ACS Publications website at DOI: 10.1021/acs.jpclett.8b00914.

(1) Additional HAAD-STEM and GPA images of nanorods with 5.0 nm cores; (2) HRTEM images of 5.0 nm CdSe cores; (3) additional HAAD-STEM and GPA images of nanorods with 2.0 nm cores; (4) pair distribution functions for CdSe cores and CdSe/CdS core/shell nanorods; (5) photoluminescence quantum yields and recombination rates for CdSe/CdS core/shell nanorods with different sizes (PDF)

AUTHOR INFORMATION

Corresponding Authors
*E-mail: arnaud.demortiere@energie-rs2e.com.
*E-mail: mpelton@umbc.edu.

ORCID Ⓘ
Valeri Petkov: 0000-0002-6392-7589
Karena Chapman: 0000-0002-8725-5633
Matthew Pelton: 0000-0002-6370-8765
Elena V. Shevchenko: 0000-0002-5565-2060

Notes
The authors declare no competing financial interest.

ACKNOWLEDGMENTS

REFERENCES

(1) Lan, X.; Masala, S.; Sargent, E. H. Charge-Extraction Strategies for Colloidal Quantum Dot Photovoltaics. *Nat. Mater.* **2014**, *13*, 233−240.

(2) Kamat, P. V. Quantum Dot Solar Cells. Semiconductor Nanocrystals as Light Harvesters. *J. Phys. Chem. C* **2008**, *112*, 18737−18753.

(3) Resch-Genger, U.; Grabolle, M.; Cavaliere-Jaricot, S.; Nitschke, R.; Nann, T. Quantum Dots Versus Organic Dyes as Fluorescent Labels. *Nat. Methods* **2008**, *5*, 763−775.

(4) Hines, M. A.; Guyot-Sionnest, P. Synthesis and Characterization of Strongly Luminescing ZnS-Capped CdSe Nanocrystals. *J. Phys. Chem.* **1996**, *100*, 468−471.

(5) Peng, X.; Schlamp, M. C.; Kadavanich, A. V.; Alivisatos, A. P. Epitaxial Growth of Highly Luminescent CdSe/CdS Core/Shell Nanocrystals with Photostability and Electronic Accessibility. *J. Am. Chem. Soc.* **1997**, *119*, 7019−7029.

(6) Ghosh Chaudhuri, R.; Paria, S. Core/Shell Nanoparticles: Classes, Properties, Synthesis Mechanisms, Characterization, and Applications. *Chem. Rev.* **2012**, *112*, 2373−2433.

(7) Deka, S.; Quarta, A.; Lupo, M. G.; Falqui, A.; Boninelli, S.; Giannini, C.; Morello, G.; De Giorgi, M.; Lanzani, G.; Spinella, C.; Cingolani, R.; Pellegrino, T.; Manna, L. CdSe/CdS/ZnS Double Shell Nanorods with High Photoluminescence Efficiency and Their Exploitation As Biolabeling Probes. *J. Am. Chem. Soc.* **2009**, *131*, 2948−2958.

(8) Chen, O.; Zhao, J.; Chauhan, V. P.; Cui, J.; Wong, C.; Harris, D. K.; Wei, H.; Han, H.-S.; Fukumura, D.; Jain, R. K.; Bawendi, M. G. Compact High-Quality CdSe−CdS Core−Shell Nanocrystals with Narrow Emission Linewidths and Suppressed Blinking. *Nat. Mater.* **2013**, *12*, 445−451.

(9) Pal, B. N.; Ghosh, Y.; Brovelli, S.; Laocharoensuk, R.; Klimov, V. I.; Hollingsworth, J. A.; Htoon, H. 'Giant' CdSe/CdS Core/Shell Nanocrystal Quantum Dots As Efficient Electroluminescent Materials: Strong Influence of Shell Thickness on Light-Emitting Diode Performance. *Nano Lett.* **2012**, *12*, 331−336.

(10) Fitzgerald, E. A.; Samavedam, S. B.; Xie, Y. H.; Giovane, L. M. Influence of Strain on Semiconductor Thin Film Epitaxy. *J. Vac. Sci. Technol., A* **1997**, *15*, 1048−1056.

(11) Adachi, S. *Properties of Semiconductor Alloys: Group-IV, III-V and II-VI Semiconductors*; John Wiley & Sons: West Sussex, U.K., 2009; Vol. *28*.

(12) Eisenberg, H. R.; Kandel, D. Formation, Ripening, and Stability of Epitaxially Strained Island Arrays. *Phys. Rev. B: Condens. Matter Mater. Phys.* **2005**, *71*, 115423.

(13) Shchukin, V.; Ledentsov, N. N.; Bimberg, D. *Epitaxy of Nanostructures*; Springer Science & Business Media: Berlin, Germany, 2013.

(14) Kwon, S. G.; Krylova, G.; Phillips, P. J.; Klie, R. F.; Chattopadhyay, S.; Shibata, T.; Bunel, E. E.; Liu, Y.; Prakapenka, V. B.; Lee, B.; Shevchenko, E. V. Heterogeneous Nucleation and Shape Transformation of Multicomponent Metallic Nanostructures. *Nat. Mater.* **2015**, *14*, 215−223.

(15) Yang, S.; Prendergast, D.; Neaton, J. B. Strain-Induced Band Gap Modification in Coherent Core/Shell Nanostructures. *Nano Lett.* **2010**, *10*, 3156−3162.

(16) Ithurria, S.; Guyot-Sionnest, P.; Mahler, B.; Dubertret, B. Mn^{2+} as a Radial Pressure Gauge in Colloidal Core/Shell Nanocrystals. *Phys. Rev. Lett.* **2007**, *99*, 265501.

(17) Tschirner, N.; Lange, H.; Schliwa, A.; Biermann, A.; Thomsen, C.; Lambert, K.; Gomes, R.; Hens, Z. Interfacial Alloying in CdSe/CdS Heteronanocrystals: A Raman Spectroscopy Analysis. *Chem. Mater.* **2012**, *24*, 311−318.

(18) Gong, K.; Kelley, D. F. Lattice Strain Limit for Uniform Shell Deposition in Zincblende CdSe/CdS Quantum Dots. *J. Phys. Chem. Lett.* **2015**, *6*, 1559−1562.

(19) Gong, K.; Kelley, D. F. A Predictive Model of Shell Morphology in CdSe/CdS Core/Shell Quantum Dots. *J. Chem. Phys.* **2014**, *141*, 194704.

(20) McBride, J.; Treadway, J.; Feldman, L. C.; Pennycook, S. J.; Rosenthal, S. J. Structural Basis for Near Unity Quantum Yield Core/Shell Nanostructures. *Nano Lett.* **2006**, *6*, 1496−1501.

(21) Chen, X.; Lou, Y.; Samia, A. C.; Burda, C. Coherency Strain Effects on the Optical Response of Core/Shell Heteronanostructures. *Nano Lett.* **2003**, *3*, 799−803.

(22) Talapin, D. V.; et al. Seeded Growth of Highly Luminescent CdSe/CdS Nanoheterostructures with Rod and Tetrapod Morphologies. *Nano Lett.* **2007**, *7*, 2951−2959.

(23) She, C.; Bryant, G. W.; Demortière, A.; Shevchenko, E. V.; Pelton, M. Controlling the Spatial Location of Photoexcited Electrons in Semiconductor CdSe/CdS Core/Shell Nanorods. *Phys. Rev. B: Condens. Matter Mater. Phys.* **2013**, *87*, 155427.

(24) She, C.; Demortière, A.; Shevchenko, E. V.; Pelton, M. Using Shape to Control Photoluminescence from CdSe/CdS Core/Shell Nanorods. *J. Phys. Chem. Lett.* **2011**, *2*, 1469−1475.

(25) Hartel, P.; Rose, H.; Dinges, C. Conditions and Reasons for Incoherent Imaging in STEM. *Ultramicroscopy* **1996**, *63*, 93−114.

(26) Pennycook, S. J. Z-Contrast STEM for Materials Science. *Ultramicroscopy* **1989**, *30*, 58−69.

(27) Bertoni, G.; Grillo, V.; Brescia, R.; Ke, X.; Bals, S.; Catellani, A.; Li, H.; Manna, L. Direct Determination of Polarity, Faceting, and Core Location in Colloidal Core/Shell Wurtzite Semiconductor Nanocrystals. *ACS Nano* **2012**, *6*, 6453−6461.

(28) Hughes, S. M.; Alivisatos, A. P. Anisotropic Formation and Distribution of Stacking Faults in II−VI Semiconductor Nanorods. *Nano Lett.* **2013**, *13*, 106−110.

(29) Chung, J.; Lian, G.; Rabenberg, L. Practical and Reproducible Mapping of Strains in Si Devices Using Geometric Phase Analysis of Annular Dark-Field Images From Scanning Transmission Electron Microscopy. *IEEE Electron Device Lett.* **2010**, *31*, 854−856.

(30) Huxter, V. M.; Lee, A.; Lo, S. S.; Scholes, G. D. CdSe Nanoparticle Elasticity and Surface Energy. *Nano Lett.* **2009**, *9*, 405−409.

(31) Lu, L.; Chen, X.; Huang, X.; Lu, K. Revealing the Maximum Strength in Nanotwinned Copper. *Science* **2009**, *323*, 607−610.

(32) Wei Wang, J.; Narayanan, S.; Yu Huang, J.; Zhang, Z.; Zhu, T.; Mao, S. X. Atomic-Scale Dynamic Process of Deformation-Induced Stacking Fault Tetrahedra in Gold Nanocrystals. *Nat. Commun.* **2013**, *4*, 2340.

(33) Meng, F.; Estruga, M.; Forticaux, A.; Morin, S. A.; Wu, Q.; Hu, Z.; Jin, S. Formation of Stacking Faults and the Screw Dislocation-Driven Growth: A Case Study of Aluminum Nitride Nanowires. *ACS Nano* **2013**, *7*, 11369−11378.

(34) Hÿtch, M. J.; Snoeck, E.; Kilaas, R. Quantitative Measurement of Displacement and Strain Fields from HREM Micrographs. *Ultramicroscopy* **1998**, *74*, 131−146.

(35) Qiu, X.; Thompson, J. W.; Billinge, S. J. L. PDFgetX2: a GUI-Driven Program to Obtain the Pair Distribution Function from X-ray Powder Diffraction Data. *J. Appl. Crystallogr.* **2004**, *37*, 678−678.

(36) Farrow, C. L.; Juhas, P.; Liu, J. W.; Bryndin, D.; Božin, E. S.; Bloch, J.; Proffen, Th.; Billinge, S. J. L. PDFfit2 and PDFgui: Computer Programs for Studying Nanostructure in Crystals. *J. Phys.: Condens. Matter* **2007**, *19*, 335219.